

Adaptive Control of a Soft Continuum Manipulator

Amirhossein Kazemipour^{1,2}, Oliver Fischer¹, Yasunori Toshimitsu^{1,3}, Ki Wan Wong¹, Robert K. Katzschmann¹

Abstract—Soft robots are made of compliant and deformable materials and can perform tasks challenging for conventional rigid robots. The inherent compliance of soft robots makes them more suitable and adaptable for interactions with humans and the environment. However, this preeminence comes at a cost: their continuum nature makes it challenging to develop robust model-based control strategies. Specifically, an adaptive control approach addressing this challenge has not yet been applied to physical soft robotic arms. This work presents a reformulation of dynamics for a soft continuum manipulator using the Euler-Lagrange method. The proposed model eliminates the simplifying assumption made in previous works and provides a more accurate description of the robot’s inertia. Based on our model, we introduce a task-space adaptive control scheme. This controller is robust against model parameter uncertainties and unknown input disturbances. The controller is implemented on a physical soft continuum arm. A series of experiments were carried out to validate the effectiveness of the controller in task-space trajectory tracking under different payloads. The controller outperforms the state-of-the-art method both in terms of accuracy and robustness. Moreover, the proposed model-based control design is flexible and can be generalized to any continuum robotic arm with an arbitrary number of continuum segments.

I. INTRODUCTION

Soft robotics is an emerging sub-field of robotics that has gained much attention in recent years. Fabricated with compliant and deformable materials, soft robots can perform tasks that would be extremely challenging for conventional rigid robots [1]. What makes soft manipulators particularly interesting is that their inherent compliance makes them more suitable for human-robot interactions and compliant operations with the environment [2]. Their continuum properties also enable them to adapt to complex environments where rigid robots may fail [3].

However, this preeminence comes at a cost: their continuum nature makes it also complicated to develop model-based control strategies. The dynamic model of rigid robots can be completely written with rigid body dynamics equations, and an extensive array of model-based controllers have been proposed for them [4]. While the state of rigid robots can be uniquely described using their joint states, there is yet not even a clear consensus on a modeling approach for such highly redundant, soft-bodied continuum manipulators; multiple approaches have been proposed [5]–[9].

One approach to the dynamic modeling of a soft robotic arm is the *Koopman Operator theory* [5], [10], a data-driven

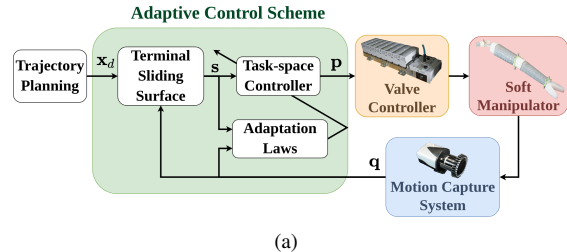


Fig. 1. The soft arm is controlled using a model-based adaptive control strategy, as illustrated in the figure. This robot is actuated using a proportional valve controller, and the motion capture cameras are used to measure its curvature.

method relying only on the measurements of the actual robot and dropping the physical simplifying assumptions of other analytical models. However, this approach requires intensive data collection to capture the whole dynamics of the robot. Other dynamic modeling methods include reduced-order FEM-based models [6], polynomial curvature fitting [11], and discrete Cosserat rod models [8]. To achieve an analytic design for model-based controllers, some researchers focused on reducing dimensions to obtain finite-dimensional models for continuum manipulators. A well-established reduced-order kinematic model is based on the *Piecewise Constant Curvature* (PCC) approach [12]. In [7], [13], [14], the dynamic model of the soft continuum arm is derived based on an approach called *Augmented Rigid Body* formulation, where the motion of the soft robot is approximated with a classic rigid link manipulator. The obtained dynamic parameters are then transformed back into a PCC formulation for control. A model based on conventional rigid manipulators allows one to use the well-established state-of-the-art tools created for rigid body robots. However, as the number of Constant Curvature (CC) segments increases, introducing the auxiliary *rigid states* in the model significantly increases the computational burden in the controller loop. The conversion between the rigid link formulation and the soft robot also makes it difficult to derive a closed-form analytical solution for the dynamics of the soft robot. As an alternative, the dynamic equations of a soft continuum arm can be derived based on the Lagrangian approach [9], [15]. The Lagrangian approach systematically derives the closed-form dynamic equations in any generalized coordinate system, eliminating the need for using the augmented rigid states in the model. Moreover, some controllers (*e.g.*, adaptive control methods) could benefit from the symbolic representation of the dynamics, which can be efficiently derived using this

¹ ETH Zurich, Switzerland

² The Sapienza University of Rome, Italy

³ The University of Tokyo, Japan

{akazemi, olivefi, ytoshimitsu, kiwong, rkk}@ethz.ch

approach. However, the existing Lagrangian approach [9], [15] assumes the center of mass position to be located at the tip of each segment, leading to an inaccurate description of the dynamics, particularly for segments with a large length-to-diameter ratio. Thus, previous models tend to suffer from inefficiencies in the computation of the dynamic parameters and oversimplifications of the dynamic model, leading to reduced model accuracy.

Prior works on closed-loop control strategies for achieving dynamic tasks for soft robotic arm include proportional-derivative (PD) control with dynamic compensation [7], [13], [14] and FEM-based reduced-order controller [6]. However, these controllers assume to have a perfect knowledge of the dynamic model. Although already established, the dynamic models of the soft robotic arm severely suffer from different uncertainties that emerge from the inadequate approximation of the dynamic parameters, a reduced kinematic model, or un-modeled dynamics. As such, traditional state-feedback controllers may be unsatisfactory, particularly for delivering dynamic tasks. To tackle this problem, a popular adaptive control scheme introduced by Li and Slotine [16] was implemented in curvature-space for a simulated continuum soft arm [17]. Moreover, a non-singular representation of the PCC-based model is employed [18], resolving the discontinuities embedded in the previous parameterizations. However, this controller is based on the hyper-redundant *Augmented Rigid Body* formulation. Furthermore, due to complexities involved in the Augmented Rigid Body model for a 3D soft manipulator, the adaptive controller is built based on a simplified model [18], which once again suffers from the approximation of mass concentrated at the tip position. Thus, previous control methods did not consider the system uncertainties or were built based on oversimplified models, affecting the performance and robustness of the control system. Additionally, the previous adaptive control scheme presented in [17] was not validated on a physical system.

In this work, we propose a model-based control strategy to resolve the discussed shortcomings of previous works. First, the dynamic model is derived using the Lagrangian approach; hence we bypass the unnecessary transformations between PCC states and augmented rigid states, significantly reducing the execution time of the controller loop by around one order of magnitude. Moreover, the derived dynamic model drops the oversimplified assumption of having a mass concentrated at the segment's tip. Based on our model, a new task-space adaptive controller is proposed which features: 1) a terminal sliding mode manifold, improving the convergence of tracking errors; and 2) an additional adaptation law in the control scheme, making the robot robust to input disturbances without requiring a priori knowledge on the bounds of uncertainties. The main contributions of this paper are summarized as follows:

- The dynamic model for a generic soft continuum multiple segments robot is derived using the Lagrangian approach with a realistic representation of the center of mass position of segments.
- A robust adaptive task-space control scheme is pro-

posed; the robustness and finite-time convergence properties are demonstrated by the Lyapunov analysis.

- The physical implementation of the proposed adaptive control strategy to a real soft robotic arm is presented – showing the performance and robustness of the controller under different load conditions.

II. MODELING

A. Kinematic model based on a Piecewise Constant Curvature

To describe the kinematics of the soft robotic arm, we use the PCC approach [12]. Consider the base frame $\{S_0\}$ followed by n reference frames $\{S_1\}, \dots, \{S_n\}$ attached at the tips of each segment. The forward kinematics can be obtained using n homogeneous transformation matrices, mapping each reference frame to the succeeding one in the open chain. Figures 2(a) and 2(b) show the kinematic representation of CC continuum segments. Under the assumption of zero elongation of the arm's segments, the configuration of each segment can be described using only two variables: the angle ϕ between the plane $x - z$ and the plane on which the curvature takes place, and θ which is the angle of curvature. The curvature of each segment satisfies the linear relation $\rho = L/\theta$, where L is the segment's length which is assumed to be constant. We denote $\mathbf{q}_i = (\phi_i \ \theta_i)^T \in \mathbb{R}^2$ the configuration of each segment, and for the whole robot, $\mathbf{q} \in \mathbb{R}^{2n}$ contains \mathbf{q}_i for all n segments.

The position and orientation of two consecutive reference frames $\{S_{i-1}\}$ and $\{S_i\}$ can be obtained using geometrical considerations [7]:

$${}^{i-1}\mathbf{T}_i(\phi_i, \theta_i) = \begin{pmatrix} {}^{i-1}\mathbf{R}_i(\phi_i, \theta_i) & {}^{i-1}\mathbf{t}_i(\phi_i, \theta_i) \\ \mathbf{0} & 1 \end{pmatrix} \quad (1)$$

where

$${}^{i-1}\mathbf{R}_i(\phi_i, \theta_i) = \begin{pmatrix} c^2\phi_i(c\theta_i - 1) + 1 & s\phi_i c\phi_i(c\theta_i - 1) & -c\phi_i s\theta_i \\ s\phi_i c\phi_i(c\theta_i - 1) & c^2\phi_i(1 - c\theta_i) + c\theta_i & -s\phi_i s\theta_i \\ c\phi_i s\theta_i & s\phi_i s\theta_i & c\theta_i \end{pmatrix} \quad (2)$$

and

$${}^{i-1}\mathbf{t}_i(\phi_i, \theta_i) = \frac{L_i}{\theta_i} (c\phi_i(c\theta_i - 1) \quad s\phi_i(c\theta_i - 1) \quad s\theta_i)^T \quad (3)$$

Note that the compact notations $s\theta_i = \sin(\theta_i)$, and $c\theta_i = \cos(\theta_i)$ are used.

B. Dynamic model based on the Lagrangian approach

The Lagrangian is defined as:

$$\mathcal{L}(\mathbf{q}, \dot{\mathbf{q}}) = \mathcal{T}(\mathbf{q}, \dot{\mathbf{q}}) - \mathcal{U}(\mathbf{q}) \quad (4)$$

where \mathcal{T} and \mathcal{U} denote the total kinetic and potential energy, respectively. The Euler-Lagrange equations of motion for a robot can be derived from the principle of least action and are represented as follows [19]:

$$\frac{d}{dt} \frac{\partial \mathcal{L}}{\partial \dot{q}_i} - \frac{\partial \mathcal{L}}{\partial q_i} = u_i, \quad i = 1, \dots, 2n \quad (5)$$

where u_i denotes the generalized force performing work on the generalized coordinates $q_i \in \mathbb{R}^{2n}$ and n denotes the total

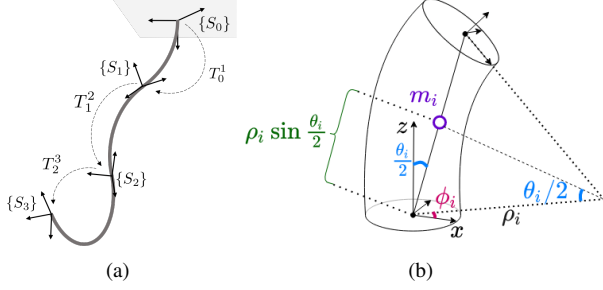


Fig. 2. The kinematic representation. (a) An example of a 3D Piecewise Constant Curvature continuum robot made of three constant curvature segments. (b) Geometric relationship of a Constant Curvature segment.

number of continuum segments. We note that the generalized coordinates used here are the PCC parameterizations (ϕ_i, θ_i) characterizing the constant curvature of each segment.

1) *Potential Energy*: The total potential energy $\mathcal{U}(\mathbf{q})$ includes both the elastic $\mathcal{U}_e(\mathbf{q})$ and gravitational $\mathcal{U}_g(\mathbf{q})$ potential energies of each continuum segment.

$$\mathcal{U} = \mathcal{U}_e + \mathcal{U}_g \quad (6)$$

The elastic potential energy can be computed as:

$$\mathcal{U}_e = \sum_{i=1}^n \mathcal{U}_{e,i} = \frac{1}{2} \sum_{i=1}^n k_{s,i} \theta_i^2 \quad (7)$$

where $k_{s,i}$ is the stiffness coefficient of the i -th segment and θ_i is the curvature angle. The gravitational potential energy can be expressed as:

$$\mathcal{U}_g = \sum_{i=1}^n \mathcal{U}_{g,i} = - \sum_{i=1}^n m_i \mathbf{g}_0^T \mathbf{r}_{0,ci} \quad (8)$$

where m_i is the mass and $\mathbf{r}_{0,ci}$ is the center of mass position of the i -th segment. \mathbf{g}_0 is the gravity acceleration vector in the base reference frame (assuming z being the vertical axis) and is represented as:

$$\mathbf{g}_0 = (0 \quad 0 \quad -g)^T \quad (9)$$

in which $g > 0$ is the gravitational acceleration constant.

2) *Center of Mass Position*: $\mathbf{r}_{0,ci}$ denotes the center of mass position of the i -th segment with respect to the robot's base frame $\{S_0\}$ and can be computed as:

$$\begin{pmatrix} \mathbf{r}_{0,ci} \\ 1 \end{pmatrix} = {}^0\mathbf{T}_1(\phi_1, \theta_1) \dots {}^{i-1}\mathbf{T}_i(\phi_i, \theta_i) \begin{pmatrix} {}^i\mathbf{r}_{i,ci} \\ 1 \end{pmatrix} \quad (10)$$

where ${}^i\mathbf{r}_{i,ci}$ is the position of the center of mass of the i -th segment with respect to $\{S_i\}$ frame. ${}^i\mathbf{r}_{i,ci}$ can be expressed using geometrical considerations as (see fig. 2(b)):

$${}^i\mathbf{r}_{i,ci} = \mathbf{R}_z(\phi_i) \mathbf{R}_y\left(\frac{\theta_i}{2}\right) \begin{pmatrix} 0 \\ 0 \\ \rho_i \sin \frac{\theta_i}{2} \end{pmatrix} \quad (11)$$

where ρ_i is the curvature radius of the i -th segment.

Remark 1. In contrast to previous models [9], [15] assuming a mass located at the segment's tip, eq. (11) considers a mass

located at the centerline connecting the base and tip of each segment, leading to a more realistic representation of the center of mass position.

3) *Kinetic Energy*: The total kinetic energy $\mathcal{T}(\mathbf{q}, \dot{\mathbf{q}})$ can be derived from the individual energy terms of each segment as:

$$\mathcal{T} = \sum_{i=1}^n \frac{1}{2} m_i \mathbf{v}_{ci}^T \mathbf{v}_{ci} \quad (12)$$

where m_i denotes the mass, and \mathbf{v}_{ci} is the linear velocity of the center of mass of each segment. \mathbf{v}_{ci} can be expressed as:

$$\mathbf{v}_{ci} = \frac{\partial \mathbf{r}_{0,ci}}{\partial \mathbf{q}} \dot{\mathbf{q}} \quad (13)$$

where $\mathbf{r}_{0,ci}$ is computed in eq. (10). We note that the contributions of rotational energies are neglected in the kinetic energy as they are much smaller than the translational energies [15].

4) *Dynamic Terms*: The explicit derivation of the dynamic terms can be obtained from the computed potential and kinetic energies of the system. The elements of the inertia matrix $\mathbf{M}(\mathbf{q})$ can be obtained from the expression of the total kinetic energy \mathcal{T} in eq. (12) as:

$$M_{i,j} = \frac{\partial}{\partial \dot{q}_j} \left(\frac{\partial \mathcal{T}}{\partial \dot{q}_i} \right), \quad \forall \dot{q}_i, \dot{q}_j \in \dot{\mathbf{q}} \quad (14)$$

The gravity $\mathbf{g}(\mathbf{q})$ and elastic $\mathbf{k}(\mathbf{q})$ forces are derived from the total potential energy in eq. (6) as:

$$g_i = \frac{\partial \mathcal{U}}{\partial q_i}, \quad k_i = \frac{\partial \mathcal{U}}{\partial q_i} \quad \forall q_i \in \mathbf{q} \quad (15)$$

The i -th row of the centrifugal and Coriolis matrix $\mathbf{C}(\mathbf{q}, \dot{\mathbf{q}})$ is computed using the Christoffel symbols as:

$$c_i^T = \frac{1}{2} \dot{\mathbf{q}}^T \left(\frac{\partial \mathbf{m}_i}{\partial \mathbf{q}} + \left(\frac{\partial \mathbf{m}_i}{\partial \mathbf{q}} \right)^T - \frac{\partial \mathbf{M}}{\partial q_i} \right) \quad (16)$$

where \mathbf{m}_i is the i -th column of the inertia matrix \mathbf{M} computed in eq. (14).

To introduce the dissipative term, the damping matrix of the i -th segment can be considered as [7]:

$$\mathbf{D}_i(q_i) = k_{d,i} \begin{pmatrix} \theta_i^2 & 0 \\ 0 & 1 \end{pmatrix} \quad (17)$$

where $k_{d,i}$ is the damping factor and the full damping matrix $\mathbf{D}(\mathbf{q}) \in \mathbb{R}^{2n \times 2n}$ can be constructed by block diagonal concatenating of $\mathbf{D}_i(q_i)$. The full dynamics model takes the following form:

$$\mathbf{M}(\mathbf{q}) \ddot{\mathbf{q}} + \mathbf{C}(\mathbf{q}, \dot{\mathbf{q}}) \dot{\mathbf{q}} + \mathbf{D}(\mathbf{q}) \dot{\mathbf{q}} + \mathbf{g}(\mathbf{q}) + \mathbf{k}(\mathbf{q}) = \mathbf{A}(\mathbf{q}) \mathbf{p} + \mathbf{d} \quad (18)$$

where $\mathbf{p} \in \mathbb{R}^c$ indicates the air pressures in robot's fluidic chambers, the superscript c specifies the total number of chambers, $\mathbf{d} \in \mathbb{R}^{2n}$ denotes the unknown input disturbances, and $\mathbf{A} \in \mathbb{R}^{2n \times c}$ is the actuator mapping matrix [7]. \mathbf{A} transforms the chamber pressures to generalized forces acting on the generalized coordinates \mathbf{q} .

Remark 2. Although, for sake of simplicity, the dynamic model derived here utilizes the conventional PCC parameterization (ϕ_i, θ_i) as generalized coordinates, other improved parameterizations (e.g., in [18]) can also be employed to resolve the singularity issues when the robot is straight. Nevertheless, our model-based control scheme is still valid thanks to a singularity handling technique used in the control synthesis (check section III-B for details).

C. Linear Parameterization and Dynamic Identification

Neglecting the unknown input disturbances, the dynamic equations in eq. (18) can be re-written in a linear form as:

$$\mathbf{Y}(\mathbf{q}, \dot{\mathbf{q}}, \ddot{\mathbf{q}}) \mathbf{a} = \mathbf{A}(\mathbf{q}) \mathbf{p} \quad (19)$$

where $\mathbf{a} \in \mathbb{R}^r$ contains r number of dynamic coefficients of the robot and $\mathbf{Y} \in \mathbb{R}^{2n \times r}$ is called the *regression matrix* that is a known time-varying matrix depending only on $\mathbf{q}, \dot{\mathbf{q}}, \ddot{\mathbf{q}}$. The elements of vector \mathbf{a} are, in general, a combination of the robot's physical parameters, i.e., length, mass, stiffness, and damping coefficients of segments.

To verify the dynamic model, we need to estimate the dynamic coefficients through a set of experiments (see section IV-B.1 for details). The dynamic identification procedure can be done by collecting $N \gg n$ samples of the configuration \mathbf{q} the chamber's pressure \mathbf{p} . The velocity $\dot{\mathbf{q}}$ and the acceleration $\ddot{\mathbf{q}}$ vectors are computed off-line by numerical differentiation. For each sample $(\mathbf{p}_k, \mathbf{q}_k, \dot{\mathbf{q}}_k, \ddot{\mathbf{q}}_k)$, with $k = 1, \dots, N$, we have

$$\mathbf{Y}_k(\mathbf{q}_k, \dot{\mathbf{q}}_k, \ddot{\mathbf{q}}_k) \mathbf{a} = \mathbf{A}_k(\mathbf{q}_k) \mathbf{p}_k \quad (20)$$

Concatenating these quantities in vectors and matrices results as:

$$\bar{\mathbf{Y}} \mathbf{a} = \bar{\mathbf{A}} \bar{\mathbf{p}} \quad (21)$$

where $\bar{\mathbf{Y}} \in \mathbb{R}^{2Nn \times r}$, $\bar{\mathbf{A}} \in \mathbb{R}^{2Nn \times Nc}$, and $\bar{\mathbf{p}} \in \mathbb{R}^{Nc}$. The estimated values of the dynamic coefficients can be obtained by solving a linear least squares problem as [20]:

$$\hat{\mathbf{a}} = (\bar{\mathbf{Y}}^T \bar{\mathbf{Y}})^{-1} \bar{\mathbf{Y}}^T \bar{\mathbf{A}} \bar{\mathbf{p}} \quad (22)$$

III. CONTROL SYNTHESIS

In this section, we present the proposed adaptive control scheme for soft continuum manipulators in both the curvature space and task space.

A. Adaptive Control: Curvature Space

We first begin by introducing a modified version of the reference trajectories presented in [21], which then enables us to define a terminal sliding manifold. The proposed reference trajectories at the velocity and acceleration levels are given as follows:

$$\dot{\mathbf{q}}_r = \dot{\mathbf{q}}_d + \Lambda \text{sign}^\alpha(\mathbf{q}_d - \mathbf{q}) \quad (23)$$

$$\ddot{\mathbf{q}}_r = \ddot{\mathbf{q}}_d + \alpha \Lambda |\mathbf{q}_d - \mathbf{q}|^{\alpha-1} (\dot{\mathbf{q}}_d - \dot{\mathbf{q}}) \quad (24)$$

where \mathbf{q}_d is the desired trajectory in the configuration space, Λ is a constant diagonal matrix with positive diagonal

entries, and $\alpha \in (0.5, 1)$ is a constant scalar. Accordingly, the nonlinear terminal sliding manifold \mathbf{s} can be defined as:

$$\mathbf{s} \triangleq \dot{\mathbf{q}} - \dot{\mathbf{q}}_r = \dot{\mathbf{e}}_q + \Lambda \text{sign}^\alpha(\mathbf{e}_q) \quad (25)$$

where $\mathbf{e}_q \triangleq \mathbf{q} - \mathbf{q}_d$ and $\dot{\mathbf{e}}_q \triangleq \dot{\mathbf{q}} - \dot{\mathbf{q}}_d$. The control law is chosen as:

$$\mathbf{p} = \mathbf{A}^\dagger(\mathbf{q}) \left(\hat{\mathbf{M}}(\mathbf{q}) \ddot{\mathbf{q}}_r + \hat{\mathbf{C}}(\mathbf{q}, \dot{\mathbf{q}}) \dot{\mathbf{q}}_r + \hat{\mathbf{D}}(\mathbf{q}) \dot{\mathbf{q}} + \hat{\mathbf{g}}(\mathbf{q}) + \hat{\mathbf{k}}(\mathbf{q}) - \mathbf{K}_D \mathbf{s} - \hat{\mathbf{b}} \text{sign}(\mathbf{s}) \right) \quad (26)$$

where \mathbf{K}_D is a diagonal matrix with positive entries and $\mathbf{A}^\dagger(\mathbf{q})$ is the pseudo-inverse of the mapping matrix. The estimated feedback-linearization terms in the control law can be computed using the regressor matrix \mathbf{Y} introduced in eq. (19) as:

$$\hat{\mathbf{M}} \ddot{\mathbf{q}}_r + \hat{\mathbf{C}} \dot{\mathbf{q}}_r + \hat{\mathbf{D}} \dot{\mathbf{q}} + \hat{\mathbf{g}} + \hat{\mathbf{k}} = \mathbf{Y}(\mathbf{q}, \dot{\mathbf{q}}, \ddot{\mathbf{q}}) \hat{\mathbf{a}} \quad (27)$$

Accordingly, the control law in eq. (26) can be rewritten as:

$$\mathbf{p} = \mathbf{A}^\dagger(\mathbf{q}) \left(\mathbf{Y}(\mathbf{q}, \dot{\mathbf{q}}, \ddot{\mathbf{q}}) \hat{\mathbf{a}} - \mathbf{K}_D \mathbf{s} - \hat{\mathbf{b}} \text{sign}(\mathbf{s}) \right) \quad (28)$$

In the control synthesis, we have considered two adaptation laws. The first adaptation law is related to the estimation of uncertain dynamic coefficients in vector \mathbf{a} :

$$\dot{\hat{\mathbf{a}}} = -\Gamma \mathbf{Y}^T(\mathbf{q}, \dot{\mathbf{q}}, \ddot{\mathbf{q}}) \mathbf{s} \quad (29)$$

where $\hat{\mathbf{a}}$ is the estimation of dynamic coefficients \mathbf{a} and $\Gamma > 0$ is a diagonal constant gain matrix. The second adaptation law is designed to make the control law robust to unknown external disturbances:

$$\dot{\hat{\mathbf{b}}} = \Psi |\mathbf{s}| \quad (30)$$

where $\hat{\mathbf{b}}$ is the estimation of the upper bound of disturbances \mathbf{b} and $\Psi > 0$ is a diagonal constant gain matrix.

For convenience in the stability proof, we first give the following lemma and assumption:

Lemma 1. As the Coriolis matrix is defined using the Christoffel symbols in eq. (16), the matrix $(\dot{\mathbf{M}} - 2\mathbf{C})$ is skew-symmetric.

Assumption 1. The input disturbances \mathbf{d} are bounded by:

$$|d_i| \leq b_i, \quad i = 1, \dots, n \quad (31)$$

where b_i is an unknown positive scalar.

The stability of the control scheme can be proved by considering the following Lyapunov function:

$$V(t) = \frac{1}{2} \mathbf{s}^T \mathbf{M} \mathbf{s} + \frac{1}{2} \tilde{\mathbf{a}}^T \Gamma^{-1} \tilde{\mathbf{a}} + \frac{1}{2} \tilde{\mathbf{b}}^T \Psi^{-1} \tilde{\mathbf{b}} \quad (32)$$

where $\tilde{\mathbf{a}} = \mathbf{a} - \hat{\mathbf{a}}$ and $\tilde{\mathbf{b}} = \mathbf{b} - \hat{\mathbf{b}}$. By taking the time-derivative of $V(t)$ along with eq. (18), we obtain:

$$\begin{aligned} \dot{V} &= \frac{1}{2} \mathbf{s}^T \dot{\mathbf{M}} \mathbf{s} + \mathbf{s}^T \mathbf{M} \dot{\mathbf{s}} - \tilde{\mathbf{a}}^T \Gamma^{-1} \dot{\tilde{\mathbf{a}}} - \tilde{\mathbf{b}}^T \Psi^{-1} \dot{\tilde{\mathbf{b}}} \\ &= \frac{1}{2} \mathbf{s}^T \dot{\mathbf{M}} \mathbf{s} + \mathbf{s}^T (-\mathbf{M} \ddot{\mathbf{q}}_r - \mathbf{C} \dot{\mathbf{q}} - \mathbf{D} \dot{\mathbf{q}} - \mathbf{g} \\ &\quad - \mathbf{k} + \mathbf{d} + \mathbf{A} \mathbf{p}) - \tilde{\mathbf{a}}^T \Gamma^{-1} \dot{\tilde{\mathbf{a}}} - \tilde{\mathbf{b}}^T \Psi^{-1} \dot{\tilde{\mathbf{b}}} \end{aligned} \quad (33)$$

By replacing the control law in eq. (26) and using the relations in eq. (25) and eq. (27), we have:

$$\begin{aligned} \dot{V} &= \frac{1}{2} \mathbf{s}^T \dot{\mathbf{M}} \mathbf{s} \\ &+ \mathbf{s}^T (-\mathbf{Y} \tilde{\mathbf{a}} - \mathbf{C} \mathbf{s} - \mathbf{K}_D \mathbf{s} + \mathbf{d} - \hat{\mathbf{b}} \text{sign}(\mathbf{s})) \\ &- \tilde{\mathbf{a}}^T \mathbf{\Gamma}^{-1} \dot{\tilde{\mathbf{a}}} - \tilde{\mathbf{b}}^T \mathbf{\Psi}^{-1} \dot{\tilde{\mathbf{b}}} \end{aligned} \quad (34)$$

Replacing the adaptation laws in eq. (29) and eq. (30) yields

$$\begin{aligned} \dot{V} &= \frac{1}{2} \mathbf{s}^T (\dot{\mathbf{M}} - 2\mathbf{C}) \mathbf{s} - \mathbf{s}^T \mathbf{Y} \tilde{\mathbf{a}} - \mathbf{s}^T \mathbf{K}_D \mathbf{s} + \mathbf{s}^T \mathbf{d} \\ &- \hat{\mathbf{b}}^T |\mathbf{s}| + \tilde{\mathbf{a}}^T \mathbf{Y}^T \mathbf{s} - (\mathbf{b} - \hat{\mathbf{b}})^T |\mathbf{s}| \end{aligned} \quad (35)$$

Using the skew-symmetric property in lemma 1 and considering the relation $\mathbf{s}^T \mathbf{d} \leq |\mathbf{s}|^T \mathbf{b}$ followed by assumption 1, we get:

$$\dot{V} \leq -\mathbf{s}^T \mathbf{K}_D \mathbf{s} \leq 0 \quad (36)$$

Therefore, the proposed control law eq. (26) with the adaptation laws introduced in eqs. (29) and (30) force the trajectories to reach the sliding manifold $\mathbf{s} = 0$. When the sliding condition $\mathbf{s} = 0$ is reached, the trajectories are determined by the following differential equation:

$$\dot{e}_q = -\mathbf{\Lambda} \text{sign}^\alpha(e_q) \quad (37)$$

It is noted that for $\alpha = 1$, eq. (37) reduces to the conventional linear sliding surface $\dot{e}_q = -\mathbf{\Lambda} e_q$ used in [17], [21]. By direct integration of eq. (37), it can be shown that [22], given $e_q(0) \neq 0$, the trajectories will reach $e_q = 0$ in a finite time determined by:

$$t_{f,i} = \Lambda_i^{-1} (1 - \alpha)^{-1} |e_{q,i}(0)|^{1-\alpha} \quad (38)$$

Therefore, $e_q = 0$ is a terminal attractor, that is, the tracking errors converge to zero in finite time. It is noted that the reaching time $t_{f,i}$ depends on the initial error $e_{q,i}(0)$ and is adjustable by modulating the parameters Λ_i and α in eq. (25).

To avoid overestimation of the dynamic coefficients, we use the boundary layer technique [23] by defining a new variable as:

$$s_{\Delta i} = s_i - \phi_i \text{sat}\left(\frac{s_i}{\phi_i}\right), \quad i = 1, \dots, n \quad (39)$$

where $\phi_i > 0$ is the boundary layer thickness. The saturation function is defined as:

$$\text{sat}\left(\frac{s_i}{\phi_i}\right) = \begin{cases} \text{sign}(s_i) & \text{if } |s_i| \geq \phi_i \\ \frac{s_i}{\phi_i} & \text{if } |s_i| < \phi_i \end{cases} \quad (40)$$

The new variable $s_{\Delta i}$ features $s_{\Delta i} = 0$ inside the boundary layer ($|s_i| < \phi_i$) and outside the boundary layer, the relation $\dot{s}_{\Delta i} = \dot{s}_i$ is satisfied. Accordingly, the adaptation laws are modified as:

$$\dot{\tilde{\mathbf{a}}} = -\mathbf{\Gamma} \mathbf{Y}^T (\mathbf{q}, \dot{\mathbf{q}}, \ddot{\mathbf{q}}_r, \ddot{\mathbf{q}}_r) \mathbf{s}_{\Delta}, \quad \dot{\tilde{\mathbf{b}}} = \mathbf{\Psi} |\mathbf{s}_{\Delta}| \quad (41)$$

Furthermore, to eliminate the chattering phenomenon that is caused by the switching function in the control law, the sign function can be replaced by the saturation function defined in eq. (40).

Remark 3. Compared to adaptive controller in [17], the control law presented here has an additional term $\hat{\mathbf{b}} \text{sign}(\mathbf{s})$, which, as shown in the stability proof, can reject the bounded input disturbances. Moreover, thanks to the adaptation law in eq. (30), there is no need to acquire a priori knowledge of disturbances, the controller rejects them by adjusting the adaptive gains in the switching term.

Remark 4. By choosing the reference trajectories as in eq. (23), the resulting sliding surface in eq. (25) becomes a *Terminal Sliding Manifold* (TSM). Widely used in various applications [24], including rigid manipulators [25], TSM guarantees the convergence of tracking errors on the sliding manifold in finite-time, which is faster than the asymptotic convergence of the classic linear sliding surface used in [17], [21].

B. Adaptive Control: Task Space

The adaptive controller in section III-A can be extended also to the task space, following a similar approach as in [21]. To achieve this, we can replace the reference trajectories in eq. (23) by:

$$\dot{\mathbf{q}}_r = \mathbf{J}^\dagger (\dot{\mathbf{x}}_d + \mathbf{\Lambda} \text{sign}^\alpha(\mathbf{x}_d - \mathbf{x})) \quad (42)$$

and

$$\ddot{\mathbf{q}}_r = \mathbf{J}^\dagger \left(\ddot{\mathbf{x}}_d + \alpha \mathbf{\Lambda} |\mathbf{x}_d - \mathbf{x}|^{\alpha-1} (\dot{\mathbf{x}}_d - \dot{\mathbf{x}}) - \dot{\mathbf{J}} \dot{\mathbf{q}}_r \right) \quad (43)$$

where \mathbf{J}^\dagger stands for the pseudo-inverse of the Jacobian matrix \mathbf{J} . Accordingly, we have

$$\mathbf{s} = \dot{\mathbf{q}} - \dot{\mathbf{q}}_r = \mathbf{J}^\dagger (\mathbf{J} \dot{\mathbf{q}} - \dot{\mathbf{x}}_d + \mathbf{\Lambda} \text{sign}^\alpha(\mathbf{x} - \mathbf{x}_d)) \quad (44)$$

The structure of the controller and the adaptation law remain the same as presented in eqs. (26), (29) and (30).

For the stability proof, the same Lyapunov function in eq. (32) can be used, which results in:

$$\dot{V} \leq \bar{\mathbf{s}}^T \mathbf{H} \bar{\mathbf{s}} \leq 0 \quad (45)$$

where $\bar{\mathbf{s}} \triangleq \mathbf{J} \dot{\mathbf{q}} - \dot{\mathbf{x}}_d + \mathbf{\Lambda} \text{sign}^\alpha(\mathbf{x} - \mathbf{x}_d)$, $\mathbf{H} \triangleq \mathbf{J}^{\dagger T} \mathbf{K}_D \mathbf{J}^\dagger > 0$ are used. Therefore, the trajectories are guaranteed to reach $\bar{\mathbf{s}} = 0$. When the condition $\bar{\mathbf{s}} = 0$ is satisfied, the trajectories are determined by the following differential equation:

$$\mathbf{J} \dot{\mathbf{q}} - \dot{\mathbf{x}}_d + \mathbf{\Lambda} \text{sign}^\alpha(\mathbf{x} - \mathbf{x}_d) = 0 \quad (46)$$

Replacing the kinematic relation $\dot{\mathbf{x}} = \mathbf{J} \dot{\mathbf{q}}$ into eq. (46) yields:

$$\dot{e}_x = -\mathbf{\Lambda} \text{sign}^\alpha(e_x) \quad (47)$$

where $e_x \triangleq \mathbf{x} - \mathbf{x}_d$, $\dot{e}_x \triangleq \dot{\mathbf{x}} - \dot{\mathbf{x}}_d$. The differential equation in eq. (47) is similar to the one obtained in eq. (37). Thus, the finite time convergence of Cartesian tracking errors on the sliding manifold is guaranteed.

The PCC parameterization utilized in the kinematic model suffers from singularities [18]. In particular, when a continuum segment is stretched out ($\theta_i = 0$), the Jacobian matrix loses rank; therefore, it is necessary to employ a scheme for dealing with these singularities. To handle this issue, we used the damped pseudo-inversion approach with a variable damping factor [26]. Consider the Singular Value

Decomposition (SVD) of the Jacobian matrix, $\mathbf{J} = \mathbf{U}\mathbf{\Sigma}\mathbf{V}$, where $\mathbf{U} \in \mathbb{R}^{m \times m}$ is a unitary matrix with column vectors \mathbf{u}_i , $\mathbf{V} \in \mathbb{R}^{n \times n}$ is a unitary matrix with column vectors \mathbf{v}_i , and $\mathbf{\Sigma} \in \mathbb{R}^{m \times n}$ is a diagonal matrix containing the singular values $\sigma_i \geq 0$ of \mathbf{J} . The damped pseudo-inverse of the Jacobian matrix can be computed based on the following approximation:

$$\mathbf{J}^\dagger \simeq \mathbf{V}\mathbf{\Sigma}^\dagger\mathbf{U}^T \simeq \sum_{i=1}^r \frac{\sigma_i}{\sigma_i^2 + \lambda^2} \mathbf{v}_i \mathbf{u}_i^T \quad (48)$$

where r denotes the rank of \mathbf{J} . The damping factor λ^2 can be modulated near the singularities as:

$$\lambda^2 = \begin{cases} 0 & \text{if } \sigma_m \geq \epsilon \\ (1 - (\frac{\sigma_m}{\epsilon})^2) \lambda_{max}^2 & \text{otherwise} \end{cases} \quad (49)$$

where σ_m is the smallest singular value, $\epsilon > 0$ defines the range of damping operation, and $\lambda_{max} > 0$ is the highest damping factor applied close to singularities.

IV. EXPERIMENTAL RESULTS AND DISCUSSIONS

This section validates the model-based control scheme presented in the previous sections through physical experiments on an actual soft continuum robotic arm. We begin by first explaining the experimental setup. This is followed by the results of model identification and proposed task-space control strategy.

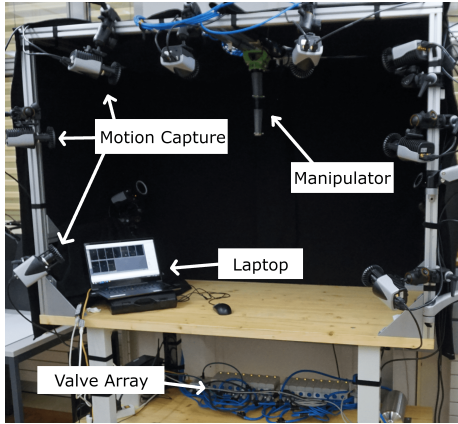


Fig. 3. The soft continuum arm consists of two segments. A valve array is used to pressurize the chambers independently. The motion capture cameras mounted on a rigid frame measure the curvature of continuum segments in real-time.

A. Experimental Setup

The experimental setup is shown in fig. 3. It consists of a soft arm with a gripper, a proportional valve manifold, and a motion capture system. The soft arm used here consists of two segments, each of which having three inflatable chambers; we refer to [27] for more details on this prototype design. The soft gripper and each of the six chambers were actuated independently through an array of proportional valves. The robot configurations were measured in real-time with a motion capture system consisting of eight IR cameras

and two RGB cameras mounted around the manipulator and connected to a laptop running a motion capture software. The reflective markers were attached to the robot base and around the tip of each segment.

To implement the adaptive proposed task-space controller, we first used MATLAB's Symbolic Math Toolbox to derive the dynamic model in explicit form based on the Lagrangian approach discussed in section II-B. The dynamic coefficients vector \mathbf{a} was then constructed by suitably choosing the parameters to achieve the linear parameterization described in eq. (19). This enabled us to generate a *c++* function for the regressor matrix \mathbf{Y} to be used within the controller loop. To compare our model with the state-of-the-art, we used the *Augment Rigid Arm* formulation described in [7]. The robot motion library called *Drake* [28] was used for this framework to calculate the *rigid states* and the corresponding dynamic terms of the rigid-equivalent model. To benchmark the task-space control, an inverse dynamics controller similar to [7] is used.

B. Experimental Validation Results

1) *Model Identification*: We have chosen the vector of dynamic coefficients as follows:

$$\mathbf{a} = (\mathbf{a}_1^T \quad \mathbf{a}_2^T)^T \in \mathbb{R}^{11 \times 1} \quad (50)$$

where

$$\mathbf{a}_1^T \triangleq (m_1 L_1^2 \quad m_2 L_1^2 \quad m_2 L_2^2 \quad m_2 L_1 L_2 \quad m_1 L_1 \quad m_2 L_1 \quad m_2 L_2)$$

$$\mathbf{a}_2^T \triangleq (k_{s,1} \quad k_{s,2} \quad k_{d,1} \quad k_{d,2}) \quad (51)$$

Since the vector \mathbf{a}_1 , which contains the masses and lengths of segments, can be evaluated through direct measurements, we need only the estimation of the unknown vector \mathbf{a}_2 , incorporating the stiffness and damping coefficients. This can be done by factorizing the regressor matrix into two parts:

$$(\mathbf{Y}_1 \quad \mathbf{Y}_2) \begin{pmatrix} \mathbf{a}_1 \\ \mathbf{a}_2 \end{pmatrix} = \mathbf{A}\mathbf{p} \quad (52)$$

The dynamic coefficients in \mathbf{a}_2 are then obtained by concatenating and solving the following equation using a least-squares technique as discussed in section II:

$$\mathbf{Y}_2 \mathbf{a}_2 = (\mathbf{A}\mathbf{p} - \mathbf{Y}_1 \mathbf{a}_1) \quad (53)$$

The data acquisition procedure was carried out to estimate the dynamic coefficients. The pressurization profiles for each chamber were considered to be periodic trajectories with different magnitudes at different frequencies to span the robot's workspace and admissible configurations as much as possible. The identified stiffness coefficients are $(k_{s,1}, k_{s,2}) = (0.124 \text{ N m}, 0.083 \text{ N m})$. The damping coefficients were estimated as $(k_{d,1}, k_{d,2}) = (0.011 \text{ N m s}, 0.009 \text{ N m s})$.

After computing the numerical values for dynamic coefficients, we validated our model by actuating the robot through pre-defined feed-forward pressures and compared the results of the simulated robot and the actual one. To do this, the

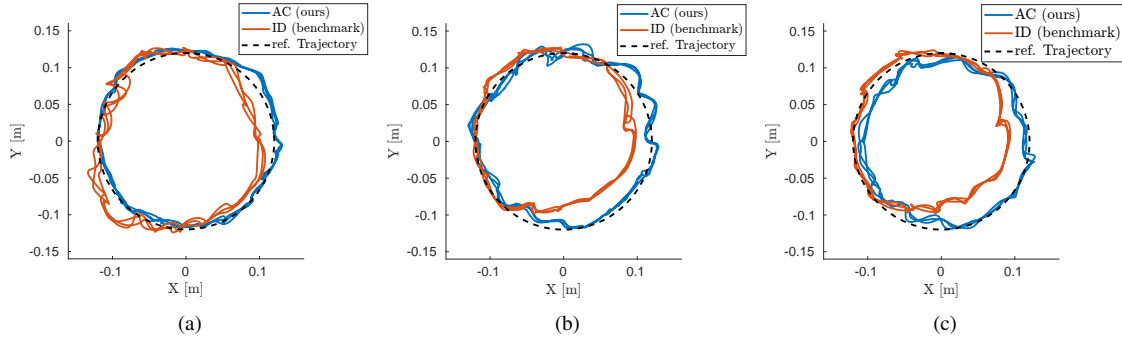


Fig. 4. Results of tracking a circular reference trajectory (dashed black line) using the proposed adaptive controller (in blue line) and the benchmark inverse dynamics controller (in red line) carrying different payloads: (a) unloaded case; (b) 11 g payload; (c) 25 g payload. The adaptive controller maintains a similar performance regardless of the payload weights, while the inverse dynamics controller performs worse even without a payload and degrades significantly when increasing the payload.

chambers of each segment were actuated according to the following sinusoidal trajectories that are:

$$p_i(t) = A \sin^2 \left(\frac{2\pi t}{T} + i \frac{2\pi}{3} \right), \quad i = 0, 1, 2 \quad (54)$$

where i denotes the index of chambers for each segment, and $A = 40$ kPa, $T = 16$ s were used. As shown in fig. 5, the resulting evolution of ϕ_i and θ_i for a simulated robot and the actual arm is overlapping well.

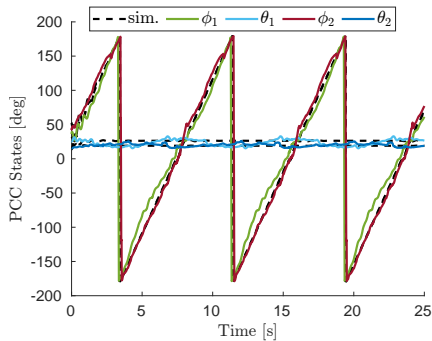


Fig. 5. The evolution of PCC parameters obtained from numerical simulation of the model and experimental results. The robot is feed-forwarded with a pre-defined pressure profiles as in eq. (54).

2) *Task-space Control*: The effectiveness of the proposed model-based control scheme is demonstrated here on an actual soft robotic arm. The parameters of the sliding surface and the controller gain are chosen as $\Lambda_i = 6.3$, $\alpha = 0.75$, and $K_{D,i} = 0.03$. The desired Cartesian trajectory was a circle in xy plane with radius of 12 cm and velocity of 0.785 rad s^{-1} . Figure 6 shows the resulting evolution of the EE tip position. It can be seen that the controller effectively tracks the Cartesian reference trajectory in all coordinates.

In order to show the robustness of the controller in handling payload mass variations, we have considered the same reference trajectory, but in this scenario, we loaded the robot with different payload masses holding by the gripper at the end-effector. The controller does not have information about the payload mass a priori. As illustrated in fig. 4, the ability of the benchmark control scheme, *i.e.*,

the inverse dynamics controller, is highly affected when the robot is loaded with a payload, and it degrades by increasing the payload mass. However, the proposed control strategy achieves higher robustness and can handle well the payload mass variations.

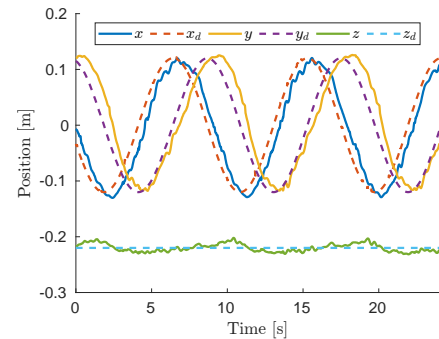


Fig. 6. Tracking of the Cartesian desired trajectory (in dashed lines) at the end effector using the adaptive control scheme.

Finally, fig. 7 shows the evolution of the execution time for our dynamic model compared to the *Augmented rigid arm formulation* implemented with the *Drake C++* library [28]. With the proposed Lagrangian-based model, the dynamic terms can be updated around one order of magnitude faster, enabling the controller loop to run at much higher frequencies.

V. CONCLUSION

This work presents a model-based control strategy that enables soft continuum robotic arms to accurately track task-space trajectories in 3D space while carrying an unknown payload mass by their end-effectors. Models that describe the compliant body of soft robotic arms have many parameters that must be identified, such as the stiffness and damping coefficients. Moreover, adding a payload to the robot changes the dynamic parameters of the model. Our generalizable adaptive controller can update such parameters online and achieve accurate control of our soft robot.

Though outperforming the current state-of-the-art method, our approach still leaves room for future improvements.

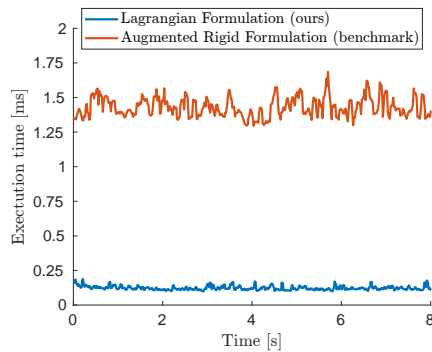


Fig. 7. Comparison of computational cost between the *Augmented rigid* model versus our Lagrangian-based model. The execution time of updating the dynamic terms in real-time for each control cycle is shown in ms.

Our adaptive control scheme does not take into account the uncertainties in the actuator mapping matrix or the presence of faults in the actuators; thus, a fault-tolerant control approach deserves investigation.

REFERENCES

- [1] D. Rus and M. T. Tolley, "Design, fabrication and control of soft robots," *Nature*, vol. 521, no. 7553, pp. 467–475, 2015, publisher: Nature Publishing Group.
- [2] R. K. Katzschmann, J. DelPreto, R. MacCurdy, and D. Rus, "Exploration of underwater life with an acoustically controlled soft robotic fish," *Science Robotics*, vol. 3, no. 16, 2018. [Online]. Available: <http://robotics.sciencemag.org/content/3/16/eaar3449>
- [3] C. Laschi, B. Mazzolai, and M. Cianchetti, "Soft robotics: Technologies and systems pushing the boundaries of robot abilities," *Science robotics*, vol. 1, no. 1, p. eaah3690, 2016.
- [4] W. K. Chung, L.-C. Fu, and T. Kröger, "Motion Control," in *Springer Handbook of Robotics*, ser. Springer Handbooks, B. Siciliano and O. Khatib, Eds. Cham: Springer International Publishing, 2016, pp. 163–194. [Online]. Available: https://doi.org/10.1007/978-3-319-32552-1_8
- [5] D. Bruder, B. Gillespie, C. D. Remy, and R. Vasudevan, "Modeling and control of soft robots using the koopman operator and model predictive control," *arXiv preprint arXiv:1902.02827*, 2019.
- [6] R. K. Katzschmann, M. Thieffry, O. Goury, A. Kruszewski, T.-M. Guerra, C. Duriez, and D. Rus, "Dynamically closed-loop controlled soft robotic arm using a reduced order finite element model with state observer," in *2019 2nd IEEE International Conference on Soft Robotics (RoboSoft)*. IEEE, 2019, pp. 717–724.
- [7] R. K. Katzschmann, C. Della Santina, Y. Toshimitsu, A. Bicchi, and D. Rus, "Dynamic motion control of multi-segment soft robots using piecewise constant curvature matched with an augmented rigid body model," in *2019 2nd IEEE International Conference on Soft Robotics (RoboSoft)*. IEEE, 2019, pp. 454–461.
- [8] J. Till, V. Aloï, and C. Rucker, "Real-time dynamics of soft and continuum robots based on cosserat rod models," *The International Journal of Robotics Research*, vol. 38, no. 6, pp. 723–746, 2019.
- [9] V. Falkenhahn, T. Mahl, A. Hildebrandt, R. Neumann, and O. Sawodny, "Dynamic modeling of constant curvature continuum robots using the euler-lagrange formalism," in *2014 IEEE/RSJ International Conference on Intelligent Robots and Systems*. IEEE, 2014, pp. 2428–2433.
- [10] D. Bruder, X. Fu, R. B. Gillespie, C. D. Remy, and R. Vasudevan, "Data-driven control of soft robots using koopman operator theory," *IEEE Transactions on Robotics*, vol. 37, no. 3, pp. 948–961, 2020.
- [11] C. Della Santina and D. Rus, "Control oriented modeling of soft robots: the polynomial curvature case," *IEEE Robotics and Automation Letters*, vol. 5, no. 2, pp. 290–298, 2019.
- [12] R. J. Webster III and B. A. Jones, "Design and kinematic modeling of constant curvature continuum robots: A review," *The International Journal of Robotics Research*, vol. 29, no. 13, pp. 1661–1683, 2010.
- [13] C. Della Santina, R. K. Katzschmann, A. Biechi, and D. Rus, "Dynamic control of soft robots interacting with the environment," in *2018 IEEE International Conference on Soft Robotics (RoboSoft)*. IEEE, 2018, pp. 46–53.
- [14] C. Della Santina, R. K. Katzschmann, A. Biechi, and D. Rus, "Model-based dynamic feedback control of a planar soft robot: trajectory tracking and interaction with the environment," *The International Journal of Robotics Research*, vol. 39, no. 4, pp. 490–513, 2020.
- [15] V. Falkenhahn, A. Hildebrandt, R. Neumann, and O. Sawodny, "Model-based feedforward position control of constant curvature continuum robots using feedback linearization," in *2015 IEEE International Conference on Robotics and Automation (ICRA)*. IEEE, 2015, pp. 762–767.
- [16] J.-J. Slotine and L. Weiping, "Adaptive manipulator control: A case study," *IEEE transactions on automatic control*, vol. 33, no. 11, pp. 995–1003, 1988.
- [17] M. Trumić, C. Della Santina, K. Jovanović, and A. Fagiolini, "Adaptive control of soft robots based on an enhanced 3d augmented rigid robot matching," *IEEE Control Systems Letters*, vol. 5, no. 6, pp. 1934–1939, 2020.
- [18] C. Della Santina, A. Bicchi, and D. Rus, "On an improved state parametrization for soft robots with piecewise constant curvature and its use in model based control," *IEEE Robotics and Automation Letters*, vol. 5, no. 2, pp. 1001–1008, 2020.
- [19] B. Siciliano, L. Sciavicco, L. Villani, and G. Oriolo, *Robotics: modelling, planning and control*. Springer Science & Business Media, 2010.
- [20] C. Gaz, M. Cognetti, A. Oliva, P. R. Giordano, and A. De Luca, "Dynamic identification of the franka emika panda robot with retrieval of feasible parameters using penalty-based optimization," *IEEE Robotics and Automation Letters*, vol. 4, no. 4, pp. 4147–4154, 2019.
- [21] J.-J. E. Slotine and W. Li, "On the adaptive control of robot manipulators," *The international journal of robotics research*, vol. 6, no. 3, pp. 49–59, 1987.
- [22] S. P. Bhat and D. S. Bernstein, "Finite-time stability of continuous autonomous systems," *SIAM Journal on Control and Optimization*, vol. 38, no. 3, pp. 751–766, 2000.
- [23] J.-J. Slotine and S. S. Sastry, "Tracking control of non-linear systems using sliding surfaces, with application to robot manipulators," *International journal of control*, vol. 38, no. 2, pp. 465–492, 1983.
- [24] X. Yu, Y. Feng, and Z. Man, "Terminal sliding mode control-an overview," *IEEE Open Journal of the Industrial Electronics Society*, 2020.
- [25] M. Zhihong, A. P. Paplinski, and H. R. Wu, "A robust mimo terminal sliding mode control scheme for rigid robotic manipulators," *IEEE transactions on automatic control*, vol. 39, no. 12, pp. 2464–2469, 1994.
- [26] A. S. Deo and I. D. Walker, "Overview of damped least-squares methods for inverse kinematics of robot manipulators," *Journal of Intelligent and Robotic Systems*, vol. 14, no. 1, pp. 43–68, 1995.
- [27] Y. Toshimitsu, K. W. Wong, T. Buchner, and R. Katzschmann, "Sopra: Fabrication and dynamical modeling of a scalable soft continuum robotic arm with integrated proprioceptive sensing," in *2021 IEEE/RSJ International Conference on Intelligent Robots and Systems (IROS)(in press)*, 2021.
- [28] R. Tedrake and the Drake Development Team, "Drake: Model-based design and verification for robotics," 2019. [Online]. Available: <https://drake.mit.edu>